university of groningen

PROBING THE THERMAL STRUCTURE IN CIRCUMSTELLAR DISKS WITH APEX

Kapteyn Astronomical Institute

July 28, 2017

Author:
Richard Kooij

Supervisors:
Prof. Dr. I. Kamp
Prof. Dr. M. R. Hogerheijde

Abstract

In this Bachelor thesis I present new APEX data on the two group II circumstellar disks HD104237 and HD142666. The aim is to infer the radial temperature distribution using the peak separation of the double-peaked Keplerian rotation line profiles of our data on the CO 6-5 rotational line, and literature data on lower rotational lines. After rebinning the data to a much lower spectral resolution, we find for HD104237 a 3σ detection. The analysis of the line profile gives a full width at half maximum of 8.6 ± 1.4 km/s, an integrated intensity of 0.25 ± 0.02 K km/s, a peak-to-peak separation of 4.4 ± 0.9 km/s, and a peak intensity of 0.034 ± 0.005 K. The inferred temperature distribution is T$\sim$ 116 K at a distance of 85 ± 50 au and T$\sim$ 33 K at a distance of 112 ± 51 au. For HD142666 the line is only detected at 2.5σ or less, which is below the threshold for a reliable result. Instead, by integrating the noise in the expected velocity range we find an upper limit of the integrated intensity of 0.20 ± 0.07 K km/s.

Contents

1 Introduction

1.1 A brief history of disks

The first hypothesis of a flattened disk as precursor to planet formation was thought up by Kant and was further developed by LaPlace already in the late 18th century. Their hypothesis arose from the structure of our own solar system, and their theory explained the observed flattened geometry and the aligned angular momenta of the Sun and the orbits of the by then known planets. Even though their theory had many flaws, their central idea still stands today. The first observational evidence of a disk structure around a star was found with mm imaging by e.g. **Beckwith et al. (1986), Beckwith and Sargent (1987)**. The images showed an extended structure around young stars and the double peaked line profiles that were found are proof of a Keplerian rotation pattern. When the Hubble Space Telescope finally launched in 1990, it opened a new window to observe protoplanetary disks. Without the issues that are faced by ground-based observatories and with an impeccable spatial resolution, it was possible to make scattered light images of nearby disks, and even detect the proplyds in the Orion nebula. With the arrival of the Atacama Large Millimeter/submillimeter Array (ALMA) in 2013 the field of protoplanetary disks is going through a revolution. Consisting of 66 twelve meter dishes combined together in an interferometric array, it provides means to spatially resolve disks on the au-scale, which will give great insight into gap-, planet-, and complex organic molecule-formation (e.g. **Lee et al. 2017, Nomura et al. 2016**).

1.2 Star and disk formation

An interstellar cloud of gas will be in hydrostatic equilibrium for as long as outward gas pressure is equal to the inward gravitational force. The condition for gravitational collapse is described by the Jeans criteria, for example the Jeans mass describes the mass above which a cloud will undergo gravitational collapse for a certain density and temperature. In an interstellar molecular cloud the Jeans mass has typical values of tens to hundreds of solar masses. This mass has to be confined inside the volume dictated by the Jeans radius. In a Giant Molecular Cloud (GMC) there are self-gravitating regions with masses up to 10^3 $M_\odot$ called clumps. These clumps contain several cores. Cores are density peaks that are likely to become a star or binary star and have masses of 0.3-10 $M_\odot$. The exact way how a core collapses is not known in full detail. In the first stage of collapse the material moves almost in free-fall. In general, cores have a non-zero angular momentum, as well as a non-negligible magnetic field. These two processes make understanding and modeling the collapse much harder. The non-zero angular momentum of

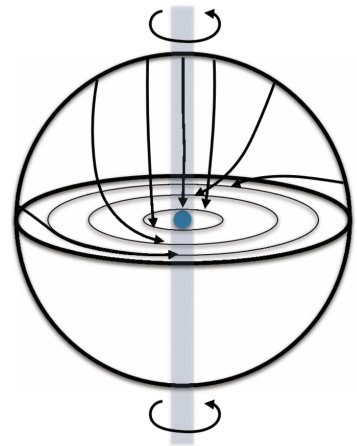

Figure 1.1: Collapse of a spherical gas envelope around a newly formed star. The arrows indicate the path of a gas parcel from different starting locations according to their specific angular momentum. Figure adopted from **Dominik (2015)**.

the core makes the material collapse to form a rotationally supported disk, see Fig. **1.1**. Material on the rotational axis has the lowest specific angular momentum and will accrete onto the center of the disk, now called a protostar. Material that is farther away from the rotation axis will instead accrete onto the disk. The gravitational energy is in this stage the main heating mechanism, until the protostar has a central temperature hot enough to start fusion reactions. We can classify protostars based on the spectral index of the overall shape of the IR spectrum,

$$\alpha \equiv \frac{d\ log(\lambda F_\lambda)}{d\ log\lambda} \quad . \tag{1.1}$$

For low mass protostars ($< 3M_\odot$) a common classification is the observed flux densities in the K band (2.2 μm) and the N band (10 μm), giving a spectral index of

$$\alpha_{K,N} = \frac{log[(\lambda F_\lambda)_{10\mu m}] - log[(\lambda F_\lambda)_{2.2\mu m}]}{log(10/2.2)} \quad . \tag{1.2}$$

We distinguish four types of protostars:

- Class 0 protostars are completely embedded and are thus heavily obscured. Their spectra therefore peak at wavelengths $\lambda > 100\mu m$. Because of the high obscuration, a characterisation by the spectral index $\alpha_{K,N}$ is not meaningful.
- Class I protostars are still embedded, but have stellar outflows and jets. This causes more power being radiated at $10\mu m$ than $2\mu m$, giving $\alpha_{K,N} > 0$.
- Class II protostars consist of a star and a disk and are named T Tauri stars. Their spectral index is $-1.5 < \alpha_{K,N} < 0$.
- Class III protostars consist of a star and a debris disk. They are still undergoing gravitational collapse, but the accretion disk is weak. They have a spectral index of $\alpha_{K,N} < -1.5$.

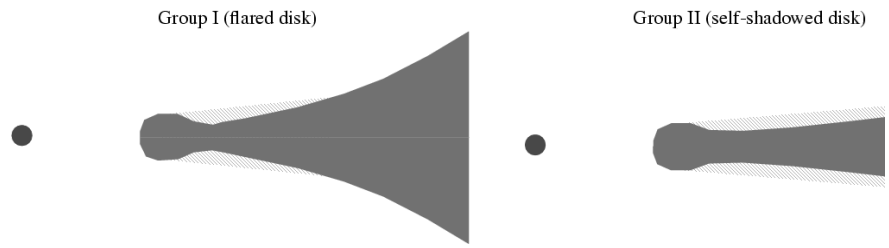

Figure 1.2: Flaring disk (left) vs. flat i.e. self-shadowed disk (right). The outer surface layers of flared disks have an increased heat absorption in comparison to self-shadowed disks. Figure adopted from **Dullemond and Dominik (2004)**.

1.3 Herbig disks

While in the process of collapse, the protostar is not yet hot enough to fuse hydrogen. Instead, it gains heat from the collapsing material. While in the pre-main sequence, we distinguish three types of protostars:

T-Tauri stars	$(M_* < 2M_\odot)$
Herbig Ae/Be stars	$(M_* \sim 2-8M_\odot)$
Massive protostars	$(M_* > 8M_\odot)$

The distinction in mass made above is of importance for the development of the star. T-Tauri stars are the least massive and therefore require more time for fusion to take place. For Herbig Ae/Be stars (first classification by **Herbig 1960**) hydrogen fusion will take place much sooner, making them much brighter than T-Tauri stars. From the Spectral Energy Distribution (SED) that we detect from these Herbig disks, we distinguish two main kinds of protoplanetary disks: Group I and Group II disks. Group I is often referred to as flaring, whereas group II disks are usually called flat or cold i.e. self-shadowing. The classification is based on the SED we detect in the mid IR. It was found by **Meeus et al. (2001)** that the SED of protoplanetary disks in this wavelength range could be fit with either a power-law, or a power-law and a black body (BB) combined. Group I disks require a BB and a power-law, whereas group II disks only need a power-law. These can be further divided into groups Ia/IIa, which contain solid state bands, and groups Ib/IIb that lack solid state bands.

The interpretation of these SEDs is however degenerate. One possible explanation is the different geometry which allows for more heat absorption in flaring disks, see Fig. **1.2**. Another is that planet formation causes gaps in the disk, where self-shadowing causes the disk to be colder, see Fig. **1.3**. Group II disks have for a long time eluded direct imaging from e.g. scattered light. This indicated that they are either very small, or large but cold. In a recent study by **Garufi et al. (2017)** it is shown that the dichotomy between the SEDs of group I and group II disks could be due to the absence or presence of a large inner cavity in the disk.

The temperature distribution in circumstellar disks can be found from the SED with numerical efforts, which can then be used to find the location of e.g. the CO ice line. The CO ice line is a region in the disk beyond which the temperature is cold enough such that CO can freeze out onto solids. Ice lines exist for several elements (e.g. H_2O, CO_2, NH_3, etc.). Icelines are of importance in the process of planet formation. Frozen out water-ice is e.g. believed to enhance the stickiness of dust grains, which can increase the rate of particle growth (e.g. **Gundlach and Blum 2015**). The increased stickiness goes hand in hand with dust coagulation, as the collisional velocities of dust grains are sufficiently low to make them stick to eachother after colliding (e.g. **Testi et al. 2014**). These processes are the first step in the formation of planetesimals and ultimately planets.

1.4 Previous work on HD104237 and HD142666

The two sources that we have data on for this thesis are the group II disks HD104237 (DX Cha) and HD142666 (V 1026 Sco). The first evidence of HD104237 being a Herbig Ae star was found by **Hu et al. (1989, 1991)**. HD104237 is the optically brightest Herbig Ae star (A4-A8Ve), and is as such an interesting object in the sky. It is at a distance of 116 ± 5 pc (**Knude and Hog 1998**), with a luminosity of 26 $L_\odot$ (**Grady et al. 2004**) and is accompanied by 5 other stars of which 2 show the characteristic IR excess associated with T Tauri stars, and has an age ≈ 5 Myr. It is still actively accreting, meaning it is highly variable in luminosity, and is one of the few Herbig stars where a bipolar microjet is observed (**Grady et al. 2004**). The inclination of the disk (i=0 is face-on) is 21 ± 4 deg (**Pogodin et al. 2015**), or 31 deg from the disk model of **Hales et al. (2014)**. HD104237 shows a very close companion at a distance of 0.2 AU, so it is in fact a binary star. The mass of the primary (HD104237A) is $2.2 \pm 0.2 M_\odot$ and the mass of the approximate spectral type K3 secondary (HD104237b) is $1.4 \pm 0.3 M_\odot$ (**Böhm et al. 2004, Garcia et al. 2013**). Simulations of the evolution of the binary system show the chaotic nature of this system in the inner 2 AU (**Dunhill et al. 2015**). The SED of HD104237 can be fit well with a non-flaring i.e. cold disk model with a radius of 90 AU and a total mass $4 \cdot 10^{-2} M_\odot$ (**Hales et al. 2014**). The predicted flatness of recent modelling of the optical to mid-IR SED of the disk by **Fang et al. (2013)** supports the classi-

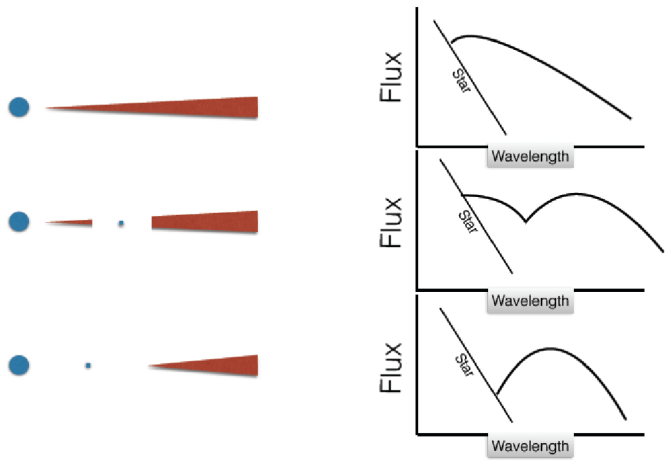

Figure 1.3: The effect of gap formation (left) on the SED (right). The gaps in the disk cause a dip in the SED at the wavelengths corresponding to the temperature the dust grains would have at that location in the disk. Figure adopted from **Waters (2015)**.

fication by **Meeus et al. (2001)** of being a group II disk. A previous detection of a CO rotational line was performed by **Hales et al. (2014)**, on the J=3-2 line.

HD142666 was first found to harbor a circumstellar disk by **Meeus et al. (1998)**. It is classified as a type II (i.e. it displays double-peaked H_α emission lines) Herbig Ae star with spectral type A7 III (**Vieira et al. 2003, Blondel and Djie 2006**). Its mass is $1.8 \pm 0.3 M_\odot$, it is at a distance of 116 pc, and it has a luminosity of 11 $L_\odot$ (**Dominik et al. 2003**). The inner disk has an inclination of $48^{+2.9}_{-3.6}$ deg (**Vural et al. 2014**), and the outer disk of 18 ± 5 deg (**Dent et al. 2005**), and a radius of the outer disk < 100 AU (**Garufi et al. 2017**). HD142666 is also actively pulsating. Even at the peak brightness of one such pulse, the reddening due to dust is significant (**Meeus et al. 1998**). This means that there must be a dusty environment around the star. Previous detections of CO rotational lines were performed by **Panić and Hogerheijde (2009)** (CO J=2-1) and by **Dent et al. (2005)** (CO J=3-2).

1.5 Aim of this research

The goal of this thesis is to analyse the data of HD104237 and HD142666. For both of these stars we want to obtain reliable line profiles that show the typical double-peaked structure from their Keplerian motion. From the line profiles we can deduce valuable parameters such as the FWHM, integrated intensity, peak intensity, and the peak-to-peak separation (Δv_{peak}). The peak-to-peak separation can be used to find the maximum radius of emission of the CO J=6-5 line. Using the maximum radius and the excitation temperature of the line as a measure of gas temperature, this can be compared to literature results of other CO rotational lines to directly infer to first order the temperature distribution in the disk. A reliable result would be a perfect way to test models like ProDiMo (**Woitke et al. 2009**). Furthermore, the temperature distribution found can be used in a much more advanced step to analyse the location of the snowlines in the disk with complex numerical codes. This can tell us much about the planet-forming capabilities of the system.

2 Theory

This chapter will go through the basic theory of the CO molecule and its transitions, primarily the rotational lines. It will also explain the characteristic Keplerian line profile and its significance.

2.1 The CO molecule

The CO molecule, after H_2, is the most abundant species in circumstellar disks which makes it a prime observational target to map the column densities throughout the disk. Another important feature of the CO molecule is that under certain conditions it can freeze out onto dust grains. This growth of dust grains is the first step in the formation of planetesimals and ultimately planets. As such, it is a key element in understanding the nature of circumstellar disks.

2.1.1 Dipole moment

Since the CO molecule consists of two atoms with a different number of protons and electrons, the molecule will have an asymmetrical charge distribution. It will therefore have a permanent dipole moment. This allows for dipole transitions to occur. H_2 has no permanent dipole moment, so dipole transitions are forbidden and are thus much less likely.

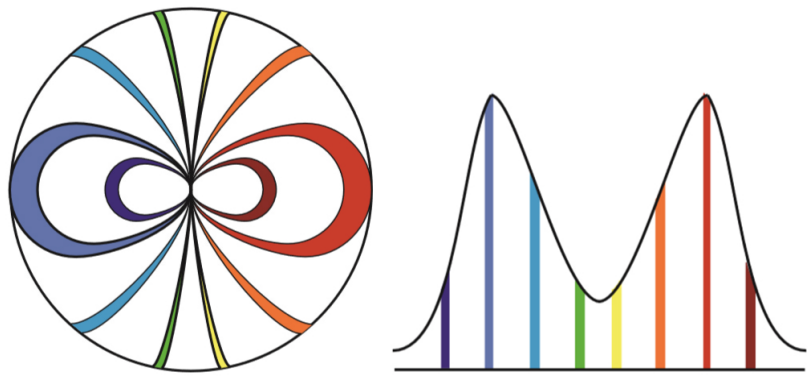

Figure 2.1: Isovelocity contours relating the peak-to-peak separation (right) to the projected velocity for an optically thick disk (left). The colours on the left indicate where (with the samen colours) the intensity is seen on the right. Figure from **Dionatos (2015)**.

2.1.2 Rotational line transitions

A molecule such as CO has the freedom to undergo rotational and vibrational motion. These motions are quantized and results in emission with typical frequencies in the near IR and (sub) mm regime. Electronic transitions are also possible, but they occur in the optical and UV regime due to higher ionization energy requirements. The total excitation energy of a molecule can thus, in terms of lowest to highest contributor, be written as

$$E_{tot} = E_{rot} + E_{vib} + E_{el} \quad . \tag{2.1}$$

For this thesis, we are interested in the CO rotational lines only.

The level energies in the rigid-rotor approximation are

$$E = \frac{h^2}{8\pi^2 I} J(J+1) \quad , \tag{2.2}$$

where E is the level energy, h is Plancks constant, I the inertia and J the rotational quantum number. The constants are then grouped together in a parameter B_0 called the rotational constant: $B_0 \equiv \frac{h}{8\pi^2 I}$ such that

$$E = hB_0 J(J+1) \quad . \tag{2.3}$$

The frequency of allowed transitions is then given by the equation

$$\nu(J \rightarrow J-1) = 2B_0 J \quad . \tag{2.4}$$

For CO, we have

$$\nu(J \rightarrow J-1) = 115.3 \cdot J \; [GHz] \quad , \tag{2.5}$$

which gives for the CO J=6-5 transition a frequency of 691.473 GHz. The Einstein A coefficient giving the rate of spontaneous decay of the CO rotational lines is given as

$$A_{J \rightarrow J-1} = \frac{2}{3} \frac{\omega^3}{\hbar c^3} \mu^2 \frac{2J}{2J+1} \; [s^{-1}] \quad , \tag{2.6}$$

where ω is the angular frequency, $\hbar$ is the reduced Planck constant, and μ is the permanent dipole moment of the CO molecule.

When a spectral observation is performed, we detect the intensity of the emission spread out over the telescope beam. This intensity is rewritten in terms of the antenna temperature as

$$T_A^* = \frac{I_\nu c^2}{2\nu^2 k_B} \quad , \tag{2.7}$$

where T_A^* is the antenna temperature, ν is the observing frequency, and k_B is Boltzmanns constant. The antenna temperature can be converted to main beam temperature via

$$T_{\rm mb} = \frac{F_{\rm eff}}{\eta_{\rm mb}} T_A^* \quad , \tag{2.8}$$

where $F_{\rm eff} = 0.95$ is the forward efficiency for APEX and $\eta_{\rm mb} = 0.60$ is the main beam efficiency, calculated from the Ruze equation given by

$$\eta(\lambda) = \eta(\infty) e^{-16\pi^2\sigma^2/\lambda^2} \quad , \tag{2.9}$$

where $\eta\ (\lambda)$ is the efficiency at wavelength λ, $\eta\ (\infty)$ the efficiency at infinity, σ the rms surface accuracy for APEX (17 μm), and λ the observing frequency.

2.2 Doppler shift and peak separation

Keplerian rotation in a circumstellar disk causes one edge to move towards us, and the other away from us. We can measure this effect via the Doppler shift of the emitted photons. The Doppler shift is given as

$$\nu_{\rm observed} = \frac{\nu_{\rm emitted}}{1 \pm \frac{v_{\rm proj}}{c}} \quad , \tag{2.10}$$

where ν is the frequency, v_{proj} is the projected velocity of the source, c is the speed of light, and where the sign in the denominator is positive for approaching sources, and negative for receding sources. This can be solved for the magnitude of the projected velocity, given the emitted and

observed frequencies. For optically thick disks, the intensity of the line profile can be directly linked to the location of the emitting region, see Fig. 2.1. The most notable implication of this is that the location of the peak intensity is related to the maximum emitting radius of the line, and hence the projected velocity at that point. This allows us to write the projected velocity as a function of the peak separation as

$$v_{proj} = \frac{\Delta v_{peak}}{2} \quad . \tag{2.11}$$

For a disk in Keplerian rotation the outer radius of the emitting area can then be found from (**Beckwith and Sargent 1993**)

$$v_{proj}(r,\theta,i) = \sqrt{\frac{GM_*}{r}} sin(i)cos(\theta) \quad , \tag{2.12}$$

where r and θ are the polar coordinates, G is the gravitational constant, M_* is the mass of the star in the center of the system, and i is the inclination of the disk. These parameters are often known from literature.

3 Observations

The observations for this study were carried out with the Atacama Pathfinder EXperiment[1] (APEX; **Güsten et al. 2006**, see sect. 3.2). The signal of CO rotational lines is expected to be very weak. Hence, the observations were executed in Beam Switch Mode. This mode measures the output powers at the defined source (ON) and a nearby reference point (OFF). The ON observation will contain emission from the source and from the continuum, whereas the OFF observation consists ideally of only continuum emission. By subtracting the OFF source from the ON source measurements, the linear drift in receiver gain and atmospheric noise are eliminated to a high degree, ensuring a flat spectral baseline.

3.1 Sources and weather conditions

The original proposal considered 8 sources, where each source would get 1.25 hours of observation time. However, a bug in the time calculation software meant that only half of the sources could be observed. HD104237 and HD142666 were given a high priority, HD144668 a medium priority and HD144432 a low priority, see Table 3.1. Due to its location on the sky and the faintness of the emission, HD104237 required much more integration time than anticipated. This meant that only the two sources named above could be observed within the ESO time granted. The final integration times for HD104237 and HD142666 were 3.7 hours and 1.3 hours, respectively. The weather conditions during the observations ranged from mediocre band 9 conditions of pwv ~0.4-0.8 [mm H_2O] to optimal conditions of pwv ~0.0-0.3 [mm H_2O]. Taken together the conditions were sufficiently good to have detected our sources. The atmospheric transmission for the APEX site at 691 GHz is 0.5-0.6 for these values of the pwv.

3.2 APEX telescope

APEX is a modified ALMA prototype antenna operating as a single dish telescope. It is often used as a precursor for ALMA observation time. It is located on a high altitude site close to ALMA in Llano de Chajnantor, Chile. The dish is 12 meter in diameter and has an rms surface accuracy of 17 microns. The FWHM of the beam is 9.0" for our observing frequency of 691.473 GHz. The sources that we are observing are much smaller, so the beam encompasses the disk.

3.2.1 SEPIA band 9 receiver

The receiver used at APEX for this study is the SEPIA Band 9 receiver. It is a dual polarisation, Double Side-Band (DSB) receiver that is built to the specifications of the ALMA band 9 with the frequency range 602-720 GHz. The average noise temperature is well below 150 K for all frequencies in this band. A complete technical description is given in **Baryshev et al. (2015)**.

3.2.2 Back-ends

The back-ends of the APEX facility are 4 XFFTS (eXtended Fast Fourier Transform Spectrometer; for a more detailed description see **Klein et al. 2012**) boards. Every board has a bandwidth of 2.5 GHz and 32768 spectral channels. The spectral resolution around our signal is 38.2 kHz, or $1.7 \cdot 10^{-2}$ km/s. There are two reasons for having 4 back-ends as opposed to 1. First, the SEPIA receiver is a dual polarisation receiver, so each polarisation needs its own back-end. Furthermore, since SEPIA B9 is a DSB receiver, the boards have a fixed overlap region of 500 MHz, centered about the rest frequency of the observation. This allows to observe the signal in the upper and lower sideband simultaneously, thereby increasing the total bandwidth to 4 GHz. During an observation, each back-end is recording the data at the same point in time. This means that the data recorded on the lower sideband will be almost the same as the data recorded on the upper sideband. They are not completely the same, since there is a spectral axis difference of half a binwidth. Since our sources are unpolarised, the data obtained from the two polarisations will be effectively independent. The data from the back-ends can therefore be added together and averaged, which enhances the signal-to-noise ratio significantly.

3.2.3 Calibration

Raw data from the APEX facility is in the Multi-Beam FITS (MBFITS) format, and is of limited use. For line obser-

[1] Based on observations with the Atacama Pathfinder EXperiment (APEX) telescope. APEX is a collaboration between the Max Planck Insitute for Radio astronomy, the European Southern Observatory, and the Onsala Space Observatory.

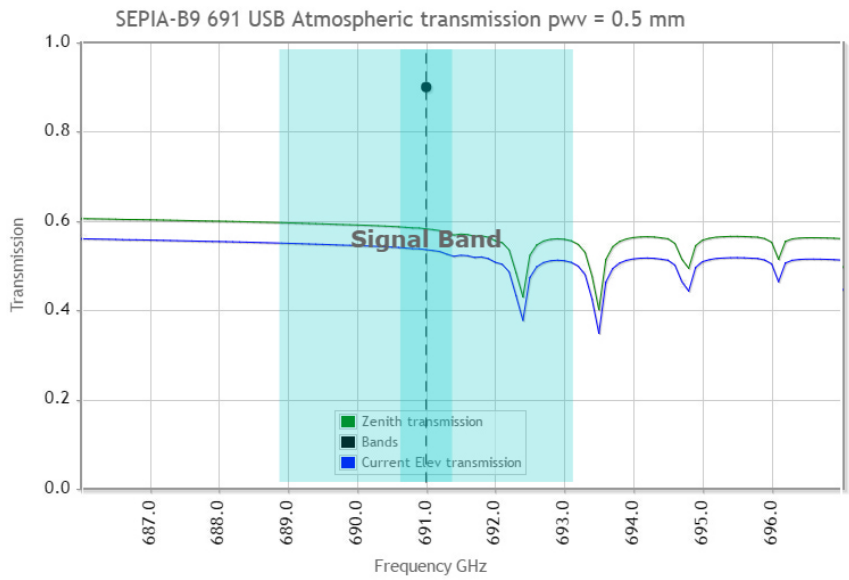

Figure 3.1: The transmission at the APEX site for the SEPIA B9 receiver for a pwv of 0.5 (mm H_2O) and for different frequencies, the light blue band being the rest frequency of the CO J=6-5 line. The green line is the tranmission at Zenith, and the blue line is the transmission at the current elevation (shown here is 60°). The dashed line is the tuning frequency, where the dot represents a transmission of 0.9.

vations the data is calibrated onsite with the OnlineCalibrator program, using a standard pipeline. The calibration pipeline follows the method described in **Polehampton and Hafok (2013)**. The calibrated data with intensity units in antenna temperature (K) are uploaded to the ESO archive.

4 Data reduction

The software used to reduce the data for this study is GILDAS[1] (Grenoble Image and Line Data Analysis Software). It is mostly used for (sub-)millimeter radioastronomical applications, for both single dish telescopes and interferometric arrays. The IRAM 30m telescope, APEX telescope and the NOrthern Extended Millimeter Array (NOEMA) provide data that is often reduced in GILDAS. The software is written mainly in FORTRAN-90/95 with some parts in C/C++. Furthermore, it provides a Python-GILDAS binding which allows for python commands within the GILDAS environment, or vice-versa. GILDAS comes with multiple packages: CLASS, GreG, ASTRO, GRAPHIC and CLIC. For our purposes, CLASS (Continuum and Line Analysis Single-dish Software) and GreG (Grenoble Graphic) are sufficient to reduce and plot the data, respectively. After the reduction it provides simple data conversion tools to save the result to .fits format which can be read using e.g. Python.

4.1 Data inspection

The data was downloaded from the ESO archive. The data file contained five calibrated '.apex' files corresponding to

[1] GILDAS is available at **http://www.iram.fr/IRAMFR/GILDAS**

Table 3.1: Shown here is a selection of group II disks with literature data on the CO J=3-2 line from **Dent et al. (2005)**, **Panić and Hogerheijde (2009)**, **Hales et al. (2014)** that were proposed to be observed with APEX SEPIA B9. Their distance range is 115-210 pc.

Run	Target	α(J2000)	δ(J2000)	ToT	Priority	Additional info
A	HD104237	12 00 05.08	-78 11 34.57	1.25	High	PWV< 0.5mm H_2O; LST=08h0016h00
A	HD142666	15 56 40.02	-22 01 40.01	1.25	High	PWV< 0.5mm H_2O; LST=12h0020h00
A	HD144432	16 06 57.95	-27 43 09.79	1.25	Low	PWV< 0.5mm H_2O; LST=12h0020h00
A	HD144668	16 08 34.29	-39 06 18.33	1.25	Medium	PWV< 0.5mm H_2O; LST=12h0020h00

the five days when our sources were observed. Included were the raw uncalibrated MB-FITS files which are of limited use as described in sect. 3.2.3. The data format '.apex' can be directly opened in CLASS. The first step is then to inspect the data file. By using the commands

$$LAS >>> file\ in\ data \tag{4.1}$$
$$LAS >>> find \tag{4.2}$$
$$LAS >>> list \tag{4.3}$$

CLASS will display a list of all observations in the current data file. The list shows key information of the scans, such as the source, the observed line and the back-end. A '.apex' file contains all sources that were observed during that particular night, including all calibration runs. Since the data has already been calibrated (see sect. 3.2.3), we have no need for this in the reduction process. So to make the reduction easier, we copied only the relevant data for each '.apex' file to a new file. This can be done as

$$LAS >>> file\ in\ data \tag{4.4}$$
$$LAS >>> list \tag{4.5}$$
$$LAS >>> find\ \backslash source\ HD104237 \tag{4.6}$$
$$LAS >>> file\ out\ hd104237\ single\ /over \tag{4.7}$$
$$LAS >>> copy \tag{4.8}$$

where command 4.6 selects only the actual observations of HD104237 excluding calibration runs. Command 4.7 opens an output file which is set to single and overwrite mode, to where command 4.8 will copy the selected data. After having copied all data to one file, the data can be inspected. The reason for inspecting the data is because there might be issues with hardware or software that leave glitches in the spectra, or cosmic rays hitting the telescope. This can be in the form of a sudden and big rise of intensity called spikes, or otherwise clearly visible artefacts. The individual spectra can be easily plotted using the commands

$$LAS >>> file\ in\ hd104237 \tag{4.9}$$
$$LAS >>> find \tag{4.10}$$
$$LAS >>> get\ first \tag{4.11}$$
$$LAS >>> plot \tag{4.12}$$
$$LAS >>> get\ next \tag{4.13}$$
$$LAS >>> plot \tag{4.14}$$

Where 4.13 and 4.14 are used iteratively to go through all spectra. The data did not show any unusually large or consistent deviation from the noise level. The data can also be viewed in full (see Fig. 4.1), where the signal strength can be visualised in a 2D color panel, where the x axis shows the velocity, and the y axis the individual spectra. A full spectrum has a very large frequency range of 2.5 GHz. Therefore, before we continue we extract the relevant part of the spectra from the full spectra. The systemic velocities with respect to the local standard of rest of our sources are 4.2 and ~ 7.0 km/s for HD104237 and HD142666, respectively. We thus expect the line to be centered about these velocities. Furthermore, we expect the line width to be typically around ~ 15 km/s. Therefore we take as new bounds -60 km/s to +60 km/s. The following class commands can achieve this.

$$LAS >>> file\ in\ hd104237 \tag{4.15}$$
$$LAS >>> find \tag{4.16}$$
$$LAS >>> file\ out\ hd104237 - ext\ single\ /over \tag{4.17}$$
$$LAS >>> extract\ '0-60'\ '0+60'\ v\ /index \tag{4.18}$$

The extracted spectra are now in the new file 'hd104237-ext.30m'. A representative spectrum is shown in Fig. 4.2 for both HD104237 and HD142666.

4.2 Removing baselines

The next step in the reduction process is to remove the baseline from all the spectra. Even though the beam switching has removed most of the continuum drift, the background emission is prone to change and can still leave unwanted deviations in the spectrum that alter the shape of the signal. First, the spectra are averaged. As explained in sect. 3.2.2, we have in our data file a combination of four different back-ends. These can all be averaged together to obtain the highest signal-to-noise ratio. The average spectrum (see Fig. 4.3) is then used to find the order of the polynomial that will fit best. We avoid altering the signal by setting a window on where we expect the signal to be. The baseline fit will ignore all channels that are inside this specified window. However, the channels inside the window will of course still be changed by subtracting the baseline fit from the spectrum. The commands for obtaining the order of the polynomial that fits the underlying continuum drift best are

$$LAS >>> file\ in\ hd104237 - ext \tag{4.19}$$
$$LAS >>> find \tag{4.20}$$
$$LAS >>> set\ unit\ v\ f \tag{4.21}$$
$$LAS >>> average \tag{4.22}$$
$$LAS >>> plot \tag{4.23}$$
$$LAS >>> set\ window\ -5\ 15 \tag{4.24}$$
$$LAS >>> draw\ window \tag{4.25}$$
$$LAS >>> base\ 1\ /pl \tag{4.26}$$
$$LAS >>> swap \tag{4.27}$$
$$LAS >>> clear\ segment \tag{4.28}$$
$$LAS >>> base\ 2\ /pl \tag{4.29}$$
$$LAS >>> plot \tag{4.30}$$

where 4.26 fits a polynomial of order 1. The baseline fit should be a low order polynomial here, because the spectra show no real sign of large continuum drifts. If however the fit is not accurate enough, it can be removed by using

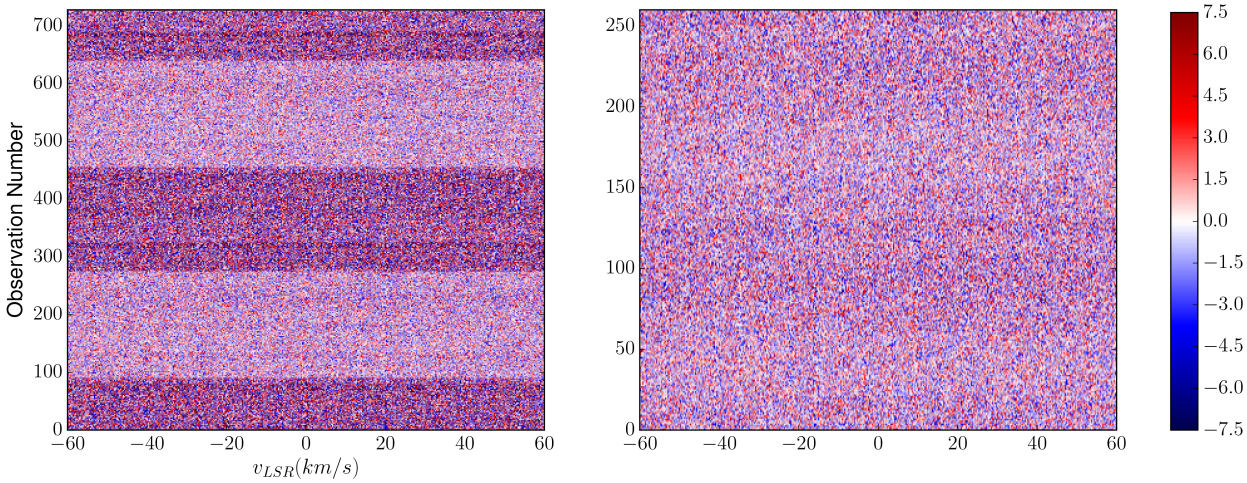

Figure 4.1: Shown here are all the observations of HD104237 (left) and HD142666 (right). Note that the lower halves are very similar to the upper halves due to 2 back-ends recording the data at the same instant of time, but with different polarizations. The color scaling as indicated by the color bar is intensity in antenna temperature (K).

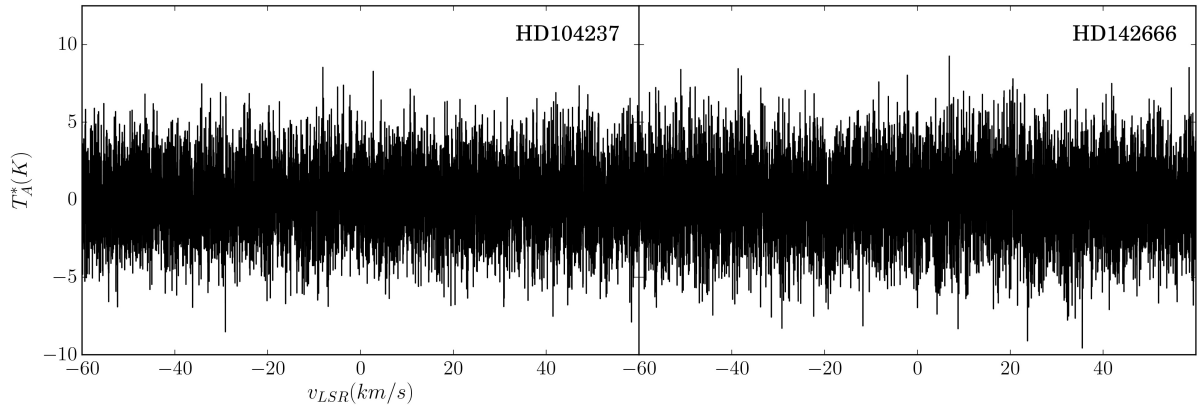

Figure 4.2: Representative spectra taken from the data of both sources in native resolution of 0.017 km/s. The scaling on the x-axis is velocity with respect to the local standard of rest, centered on the rest frequency of the CO J=6-5 line. The y-axis scaling is intensity in temperature units (K) as $T_A^* = I_\nu \frac{c^2}{2\nu^2 k}$.

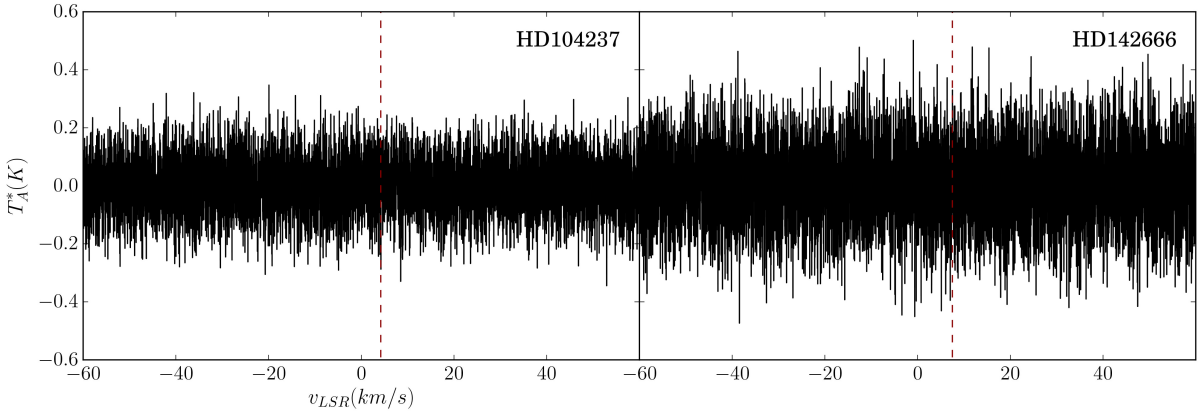

Figure 4.3: Averaged spectra for both sources. The red dashed line indicates the systemic velocity of the sources, on which we expect the signal to be centered.

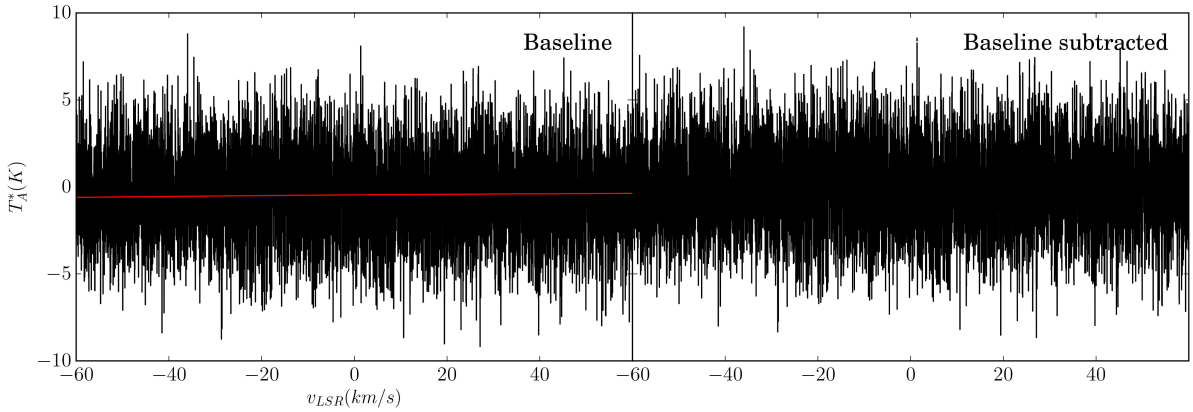

Figure 4.4: An example of a representative single spectrum to which a low-order baseline subtraction is applied.

commands 4.27 and 4.28. If the baseline fit is appropriate, which was the case for a polynomial of order 1, the baseline can be subtracted from the spectra by command 4.30.

Now that we have the order of the polynomial fit, we can apply this to all the individual spectra. This is done as follows.

$$LAS >>> file\ in\ hd104237 - ext \tag{4.31}$$
$$LAS >>> file\ out\ hd104237 - base\ single\ /over \tag{4.32}$$
$$LAS >>> find \tag{4.33}$$
$$LAS >>> set\ unit\ v\ f \tag{4.34}$$
$$LAS >>> set\ window\ -5\ 15 \tag{4.35}$$
$$LAS >>> draw\ window \tag{4.36}$$
$$LAS >>> get\ zero \tag{4.37}$$
$$LAS >>> for\ ient\ 1\ to\ found \tag{4.38}$$
$$LAS >>>:\quad get\ next \tag{4.39}$$
$$LAS >>>:\quad base\ 2 \tag{4.40}$$
$$LAS >>>:\quad write \tag{4.41}$$
$$LAS >>> next\ ient \tag{4.42}$$

After setting the window and drawing it, command 4.37 gets the first spectrum in the file. From here, commands 4.38-4.42 describe a for loop that iterates over each spectrum, applying a baseline of order 2 and writing the result to the new file. Command 4.42 will start the iteration. The baseline subtracted average spectra are shown in Fig. 4.4. Since there is no sign of a signal in the native spectral resolution for either source, we have to apply a method called smoothing to look for a weak signal.

4.3 Smoothing

CLASS has a built in smooth command. The way it works is as follows. The native spectral resolution of the APEX telescope is 38 kHz. By smoothing the spectrum, neighbouring channels are averaged and combined into one channel. This reduces the spectral resolution i.e. increases the bin size. However, if there is a weak detection buried in the noise, smoothing can enhance it due to the slightly higher average signal strength. Furthermore, because of the random nature of noise, averaging channels will also decrease the overall noise level. In CLASS the commands for smoothing a spectrum can be applied as

$$LAS >>> file\ in\ hd104237 - base \tag{4.43}$$
$$LAS >>> find \tag{4.44}$$
$$LAS >>> set\ unit\ v\ f \tag{4.45}$$
$$LAS >>> average \tag{4.46}$$
$$LAS >>> plot \tag{4.47}$$
$$LAS >>> analyse\backslash smooth\ box\ 50 \tag{4.48}$$
$$LAS >>> plot \tag{4.49}$$

where the command 4.48 takes as smoothing method 'box', which is described above, and '50' is the number of neighbouring channels that are averaged and combined. Any value may be chosen for the binning, as long as it is an integer. An example of a smoothed spectrum can be seen in Fig. 4.5. The smoothing can make some local baseline variations more apparent. For that reason, another baseline subtraction is done using the same commands as before (4.19-4.30). In these cases a higher order baseline was necessary. The order was determined by looking at the binned spectrum. Order 2 underestimated the continuum drift, whereas order 4 overestimated the continuum drift. Hence, the best fit was a polynomial of order 3. The baseline applied to a smoothed plot is shown in Fig. 4.5. The final step of the data reduction is then to write the resulting data to a Python friendly format (.fits) for further processing.

$$LAS >>> fits\ write\ hd104237.fits\ /mode\ spectrum \tag{4.50}$$

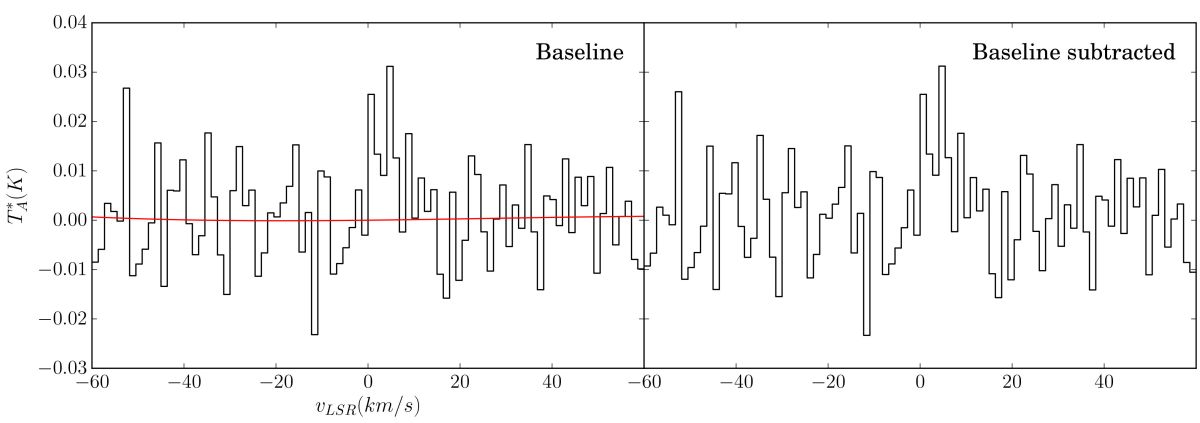

Figure 4.5: A smoothed spectrum from which another baseline is subtracted.

5 Data analysis

Due to the faintness of the detected signal, the shapes of the smoothed spectra are highly dependent on the bin size that is used. For this reason the best way to analyse the results would be to investigate as many bin sizes as we can. GILDAS CLASS only allows one to specify an integer number of neighbouring channels that will be averaged together, which limits the amount of bin sizes that can be used. Hence, to provide the best representation of the data, a Python script was written which mimicks CLASS but can rebin data to many more bin sizes. From the rebinned spectrum it subtracts a baseline of order 3. A comparison between the Python script and the method in CLASS for the same binning is shown in Fig. **5.1**. The mean difference between the methods is $\sim 8{\cdot}10^{-4}$ K, which is a few percent of the noise level and a factor three less for the signal. In general the Python script slightly undershoots (mean factor ~ 0.98) the CLASS method. We can justify the use of the Python script over the CLASS method by stating that the increase in the amount of different bin sizes that can be analysed will give us a much better idea of the shape of the signal.

5.1 Model fit

For a disk in Keplerian rotation we expect the signal to be Doppler shifted according to the projected velocities away from-, and towards us, resulting in a double-peaked profile. The magnitude of the shift for an optically thick disk depends on the maximum radius of the emitting region, and on the inclination of the disk. A proper double-peaked physical power-law fit was refrained from in this case, because the resolution is too coarse and it is unsure whether there is a double-peaked structure in the data at all. For this same reason, it was also chosen that a ProDiMo (**Woitke et al. 2009**) model fit would not be representative of the data, since it is uncertain whether there is something that requires detailed modeling. Instead, we used a fit involving the sum of two Gaussians. We assume hereby that the line shape is Gaussian in nature. The equation is written as

$$f = a \cdot e^{-\frac{(x-b)^2}{2c^2}} + a \cdot e^{-\frac{(x+b)^2}{2c^2}} \quad , \tag{5.1}$$

where a is the amplitude, b the location of the center of a peak, and c the standard deviation, see Fig. **5.2**. The location parameter b has a flipped sign for one Gaussian, causing them to be off-center, and giving the sum a double peak. The great feature about this fit is that if there is no double-peaked structure, the Python package SciPy's curvefit will set the location parameter b to very near zero, reducing the double-peaked fit to a regular Gaussian, which will be shown to occur often in the next section.

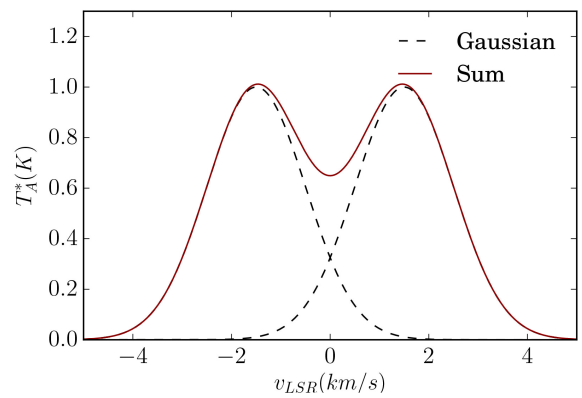

Figure 5.2: A demonstration of the applied fitting method, for parameters a = 1., b = 1.5, c = 1.

The validity of the fitting method was tested against a ProDiMo model on HD97048 and is shown in Fig. **5.3**. The found values for the FWHM are 4.23-4.52 km/s compared to their 4.10-4.23 km/s and for Δv_{peak} we find 2.28-2.35 km/s compared to their 2.4-2.5 km/s. Considering the spectral resolution of the model on HD97048, the results are in close agreement. The wings of the Gaussian profile do not match well with the ProDiMo model. However, since the signal we detect is weak, the wings of the profile will be dominated by noise and are hence indistinguishable. For the coarse resolution of the weak signal, this fit is thus sufficiently accurate.

5.2 HD104237

For HD104237, we use a simple for-loop to iterate over bin sizes ranging from 0.5-4.1 km/s with a step size of $dv = 5 \cdot 10^{-4}$ km/s. Under 0.5 km/s the data shows no sign of a signal and above 4.1 km/s the signal consists of so few points that the fit becomes inaccurate. The results are shown in Fig. **A.1**, with a stepsize of 0.5 km/s. The most common best fit model is a single Gaussian, which is of course more likely for a larger bin size.

To assess the reliability of the detection, we can look at the signal to noise ratio. The 3σ confidence level is calculated as follows. First, the mean value of the noise outside of the signal window is calculated, for which we assume that the noise is normally distributed:

$$\bar{x} = \frac{\sum_i x_i}{N} \quad . \tag{5.2}$$

From this, the standard deviation is calculated as

$$\sigma^2 = \frac{\sum_i (x_i - \bar{x})^2}{N-1} \quad . \tag{5.3}$$

The 3σ confidence level is then three times the standard deviation, corresponding to a 99.7% certainty that a signal above this level is not noise. We then set a threshold in the script that saves results if the model fit is above the 3σ level. The results that are saved include the FWHM,

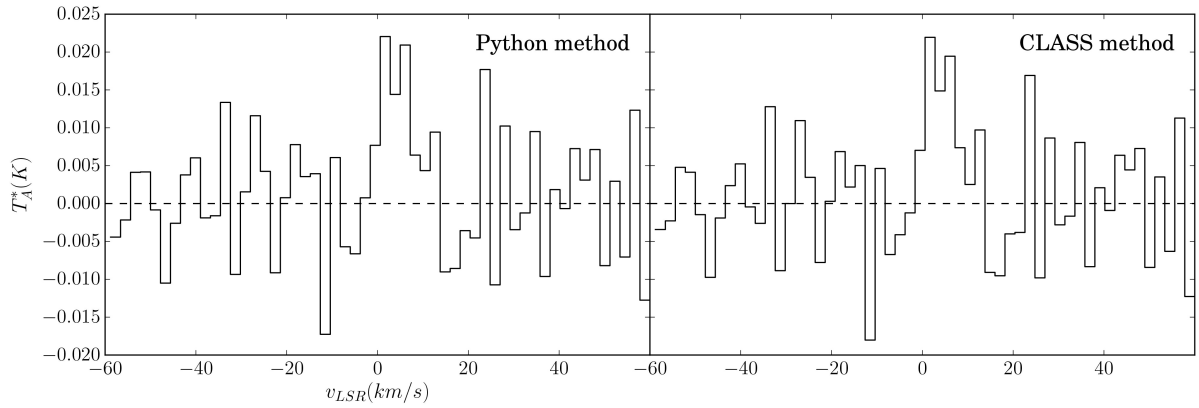

Figure 5.1: A comparison between Python and CLASS for a similar bin size of Δv = 2.2 km/s.

integrated intensity, Δv_{peak}, and the peak height. In the range of bin sizes 0.5-4.1 km/s, we find that 37% of the model fits are at or above the 3σ level. Of these 3σ results, 22% shows a double-peak structure. That 22% show a double-peaked structure even in this large range of bin sizes is rather significant. Some bin sizes that show a double-peaked structure are shown in Fig. 5.4. The reliability of this is however not as significant due to loss of structure information from the large bin sizes. The values that we find, including the 1σ uncertainties are shown in Table 5.1. The results in the table are shown for the antenna temperature, and also for the main beam temperature. The reason for correcting this is because the antenna temperature includes an integral over the main beam and all the sidelobes, whereas typically only the main beam is well known. Hence, using Eqn. 2.8, we find for the correction factor $T_{mb} = T_A^* \frac{0.95}{0.60} = 1.58 \cdot T_A^*$.

5.2.1 Gas temperature distribution in the disk

For an optically thick disk the peak-to-peak separation provides a direct measure of the outer radius of the emission region (see section 2.2). A fraction of the possible best fit models that display a peak separation of

$3\ km/s < \Delta v_{peak} < 6\ km/s$ are shown in Fig. 5.5. Peak-separations that are not in this range were considered as unphysical, because at large bin sizes the amount of data points becomes very small which makes the model fit for certain bin sizes display obviously wrong fits. To circumvent this, boundaries were set on the maximum height of the model fit and on the peak separation. If the double-peaked model fit crossed these boundaries, a single Gaussian was fit instead.

Using Eqns. 2.11, 2.12 we can estimate the maximum radius of emission, assuming that the disk is in Keplerian motion. This can be compared to the literature result of the CO J=3-2 line of HD104237, see Fig. 5.6. The radii are calculated for inclinations of i=(21,31) deg. Since the system consists of a binary star at a very close separation (0.2 au), where the radii of the stars are $\sim$ 0.01 au), we use the sum of the two masses as an approximation at the center of mass of the system, as

$$m_{\text{tot}} = m_1 + m_2 = 3.6\ M_\odot \quad . \tag{5.4}$$

We can then use the excitation temperature of the respective CO rotational lines to find the region in the disk where the temperature is sufficiently high to excite the rotational line. The parameters used and the results found are shown in Table 5.2. From the disk model of **Hales et al. (2014)**, the characteristic radius of the disk is ~90 au. The characteristic radius is where the power-law distribution in the inner region turns over to an exponential decrease for the outer region. Since CO requires a reasonably low column density to become optically thick, there can still be alot of CO emission outside the power-law region. The radii from an inclination of 21 deg are in good agreement with this. For 31 deg the radii seem to be very large. Since there should be an exponential decrease of the density after 90 au, it seems unlikely that there is still CO emission at these

Table 5.1: The results of the averaging of all the bin sizes. *corrected for T_{mb}.

Target	$FWHM$ (km/s)	$\int I_{COJ=6-5} dv$ (K km/s)	Δv_{peak} (km/s)	I_{peak} (K)
HD104237	8.6 ± 1.4	0.157 ± 0.007	4.39 ± 0.84	0.020 ± 0.003
HD104237*	8.6 ± 1.4	0.25 ± 0.02	4.39 ± 0.84	0.032 ± 0.005

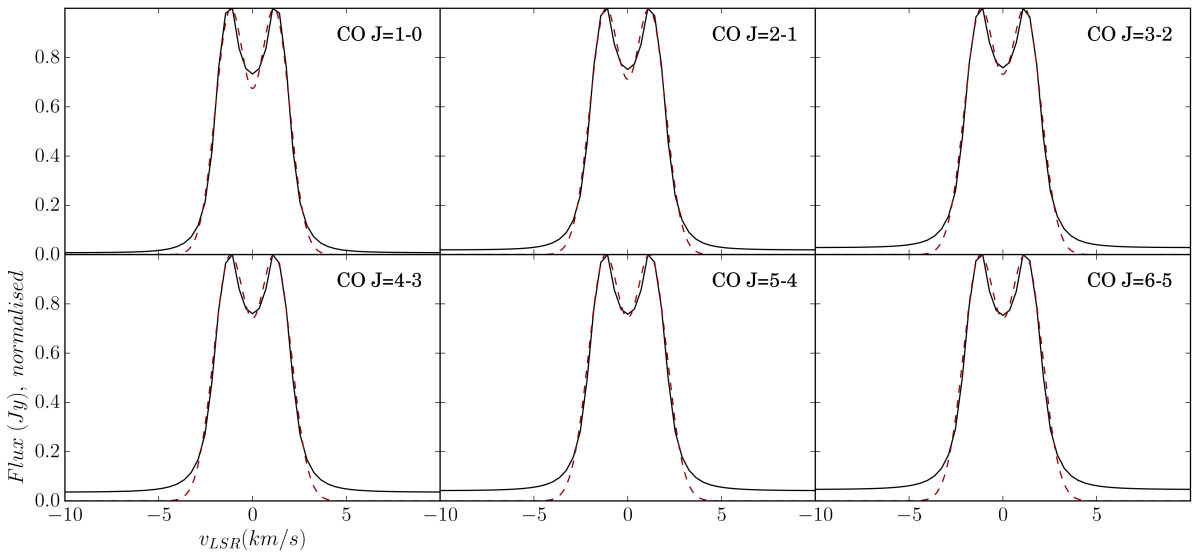

Figure 5.3: A comparison of how the fitting method works for a number of CO rotational lines as taken from a radiation thermo-chemical disk model made for the source HD97048 using ProDiMo (data courtesy of I. Kamp; see **Woitke et al. 2009**). The black line is the modeled line profile, and the red dashed line is the fit. The peak flux is normalized to 1.0 to show more clearly the differences in the fit, rather than the significant change in flux for the CO rotational lines.

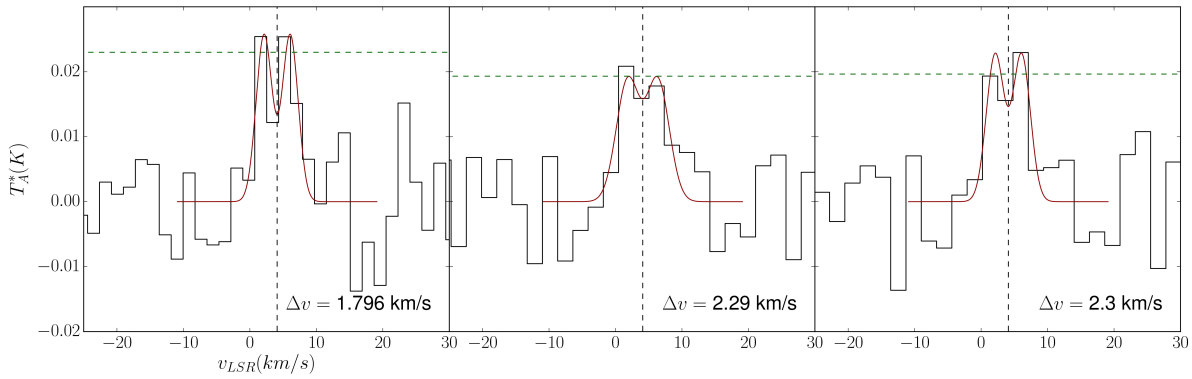

Figure 5.4: Displayed here are some bin sizes that show double-peaked fits, the y-axis shows antenna temperature (K).

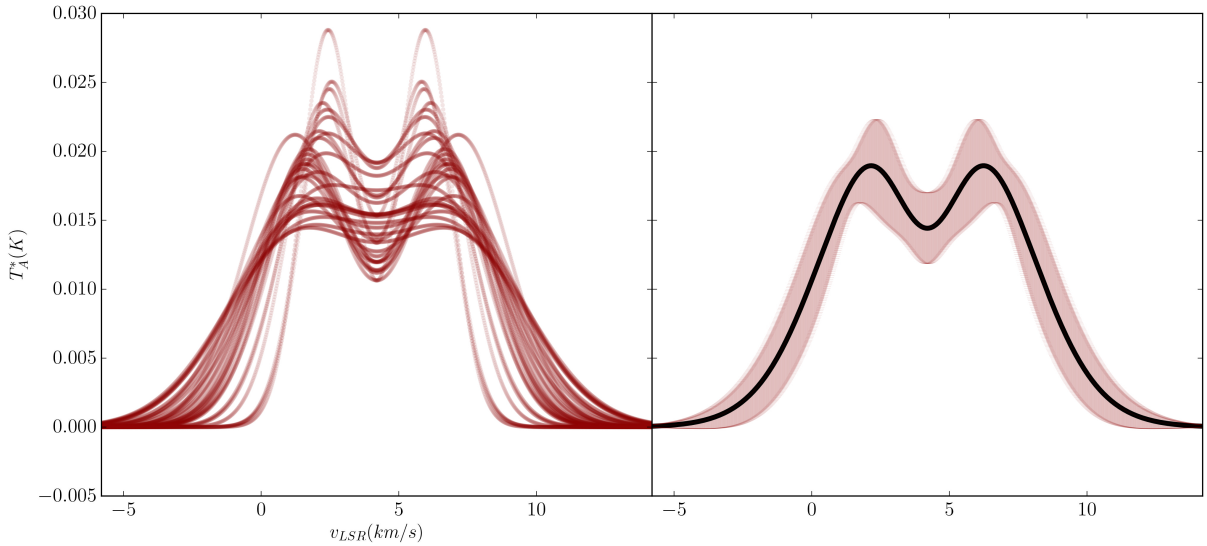

Figure 5.5: A fraction of the possible best fit models for a peak separation of 3 $km/s < \Delta v_{peak} < 6$ km/s (left), and the averaged best fit model including the 1σ level (right). Note the large spread in peak height, but relatively small spread in the peak separation.

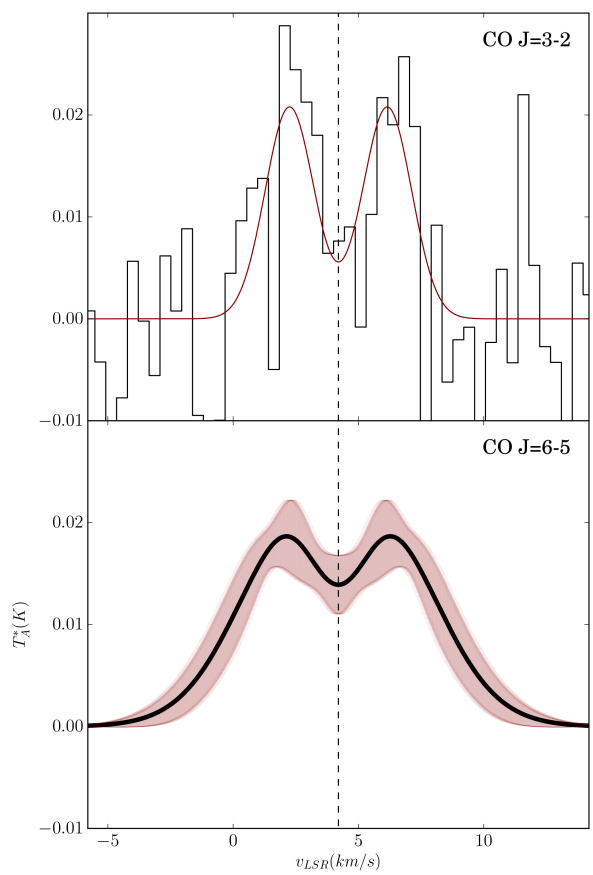

Figure 5.6: A comparison of the CO J=3-2 spectrum (data courtesy of A. Hales, see **Hales et al. 2014**) to the average best fit from ~60 double-peaked plots.

very large radii.

5.2.2 Dilution factor

The antenna temperature that we observe with the telescope consists of the source and the background. However, the beam encompasses the disk which means that the observed temperature is diluted. As a check, we can find the brightness temperature of the emitting area of the disk. The brightness temperature represents the temperature a black body in Thermal Equilibrium (TE) would have to be to reach the intensity of a grey body object at a certain frequency.

We first determine the solid angle of the disk. Assuming the emission we detect comes from a circular source at an inclination i, which traces out an ellipse, we find for the solid angle

$$\Omega_{\text{source}} = \frac{\pi R^2 sin(i)}{d^2} = 1.42 \cdot 10^{-11}\ sr \quad . \tag{5.5}$$

Where R is the maximum radius of the emitting area (R = 85 AU), d is the distance to the source (d = 116 pc), and i is the inclination (i = 21 deg). The beamsize for APEX SEPIA B9 at an observing frequency of 691.473 GHz is θ = 9.0". Assuming the beam is circular, we have that

$$\Omega_{\text{beam}} = \pi\left(\frac{\theta}{2}\right)^2 = 1.5 \cdot 10^{-9}\ sr \quad . \tag{5.6}$$

Since the antenna temperature records the temperature over the entire beam instead of just the source, we have a dilution factor given by the ratio of the solid angle subtended by the source and the beam area.

$$T_b = T_{mb} \cdot \frac{\Omega_{\text{beam}}}{\Omega_{\text{source}}} = 3.4\ K \quad , \tag{5.7}$$

where T^*_{mb} is the peak intensity. This value is quite low compared to the excitation temperature of the CO J=6-5 line. Since we have a large margin of uncertainty we can use the minimal radius that is allowed (R = 35 AU). In this case we find

$$T_b = 21\ K \tag{5.8}$$

Which is still smaller than the expected excitation temperature of 116 K. The assumptions we made (circular beam, uncertainties in the distance, inclination and radius of the source, sum of the masses of the sources), are quite significant for this calculation.

5.3 HD142666

The results of the analysis are shown in Fig. **A.2** for several bin sizes with a step size of 0.5 km/s. There is no 3σ detection of the line. This is in part attributed to the shorter integration time as compared to HD104237, but also due to HD142666 being a smaller disk (60-70 au, **Garufi et al. 2017**) than HD104237, with a characteristic radius of 90 au. A smaller disk means a smaller emitting area and hence a weaker signal. The best fit models were fit using lower boundaries on the width of the Gaussians of b=1.5. The model fits best for $v_{LSR} \approx 7.5$ km/s. To still provide a scientific result, we determine an upper limit of the integrated intensity of this line. We do this by integrating the noise for another large array of bin sizes, and average the results. The integration in this case consisted of multiplying the intensity of each bin in a velocity range of -8 - 23 km/s by the bin size that was used, as illustrated in Fig. **5.7**. We have used here the velocity range implied by **Panić and Hogerheijde (2009)** that have succesfully detected a double-peaked profile for the CO J=2-1 line. The average value within the 3σ level of the integrated intensity, corrected for T_{mb}, is 0.20 ± 0.07 K km/s.

6 Discussion

In this thesis we have presented new APEX data on the CO 6-5 rotational line on HD104237 and HD142666. The data was analysed with a primary goal of inferring the radial temperature distributions in the disks. In addition to this, some valuable parameters of the disks could also be determined. The general quality of the data obtained from APEX was good. The CO J=6-5 line emission was found to be even lower than expected.

Table 5.2: The calculated radii for the two reported inclinations, using the total mass of the system. The uncertainty in Δv_{peak} was assigned from the best-fit model on the CO J=3-2 spectrum.

HD104237	*Inclination* (deg)	Δv_{peak} (km/s)	*Mass* ($M_\odot$)	R_{max} (au)	T_{exc} (K)
CO J=6-5	21	4.4 ± 0.9	3.6	85 ± 50	116
CO J=6-5	31	4.4 ± 0.9	3.6	175 ± 82	116
CO J=3-2	21	3.8 ± 0.3	3.6	112 ± 51	33
CO J=3-2	31	3.8 ± 0.3	3.6	231 ± 65	33

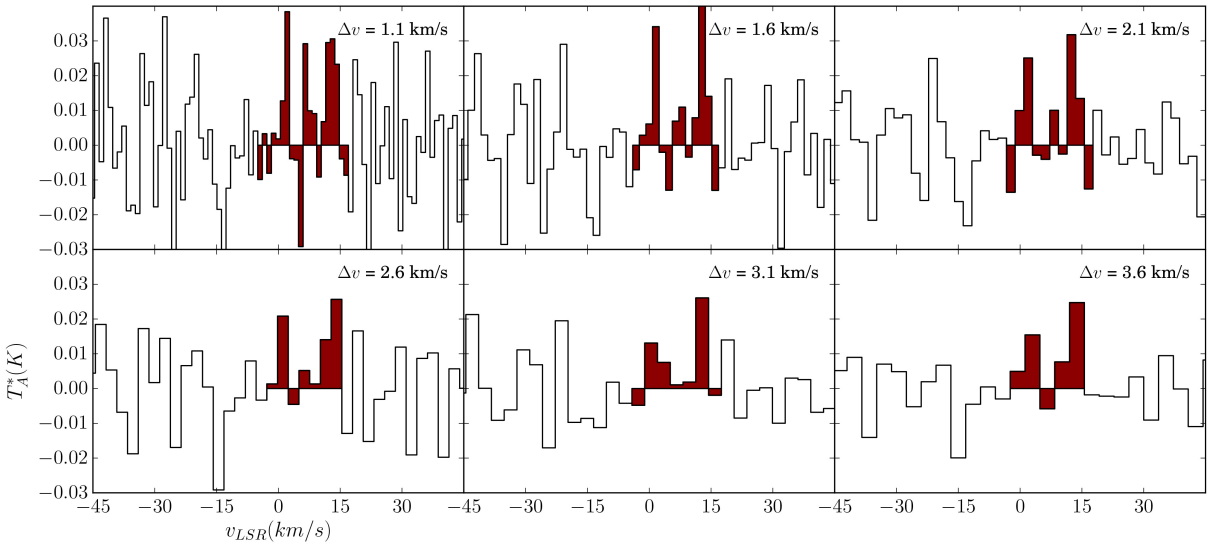

Figure 5.7: Shown here in red is the integrated intensity for the expected range of the signal of HD142666.

6.1 HD104237

For HD104237 we detect a signal at the 3σ confidence level when rebinned to > 1.5 km/s. The results we found by averaging every line profile with a 3σ result are FWHM = 8.6 ± 1.4 km/s, $\int I_{CO\ J=6-5} dv$ = 0.25 ± 0.02 K km/s, Δv_{peak} = 4.39 ± 0.84, I_{peak} = 0.034 ± 0.005 K, where the uncertainties denote the 1σ values. The reliability of the results should be interpreted with caution, due to the low resolution. A double-peaked structure was seen in 22% of the 3σ detections. Whether there really is structure in these detections is hard to say. From the peak separation of the CO J=3-2 line from literature of ~3.8 km/s we would expect the peak separation of the CO J=6-5 line to be slightly higher as it originates closer to the disk center. What is either great coincidence, or evidence of real structure, is that when we bin to ~2.1-2.3 km/s we start seeing clearly a doube-peak structure, see Fig. **5.4**. This corresponds exactly to the peak-separation that we expect from the slight increase of the literature value of the CO J=3-2 line. So there is evidence that there is indeed structure in the line profile, but the resolution is not good enough to draw a reliable conclusion. Furthermore, the low resolution eliminates the structure that we can see. Therefore, the maximum bin size that can display structure is also ~2.1-2.3 km/s, where the detection consists of three bins. Nevertheless, we used the derived peak separation to determine the outer radius of emission. The outer radii from the CO rotational lines 6-5 and the literature data of the 3-2 line are 85 ± 50 au and 112 ± 51 au. Comparison to the radial gas temperature profiles from **Fedele et al. (2016)**, Fig. 5, upper right, we find that for the uppermost CO emitting layer at z/r = 0.6 the temperature distribution that we have found is best suited for a flaring angle of ψ = 0.05. From the plot the temperatures at the radii 85 au and 112 au are 60 K and 40 K, respectively. A large value of the flaring angle causes the gas temperature to remain ~100 K for radii over 100 au, which does not seem to happen for this disk. The uncertainties in our radii are however significant. If we use the minimum radius allowed by the uncertainty, 35 au, we find a gas temperature of ~100 K. The most likely cause of this discrepancy is that we have underestimated the peak-separation because we have lost structure information by rebinning the data.

We have also calculated the brightness temperature of the CO J=6-5 emitting region using the beam dilution factor and the main beam temperature. We find for a radius of 85 au a brightness temperature of 3.4 K. This low temperature makes it likely that we have indeed underestimated the peak separation, as a smaller emitting region would give a larger brightness temperature.

6.2 HD142666

The confidence levels for a detection in HD142666 were at best ~ 2.5σ. Since the results would not be significant for a full on analysis, we refrained from this. Instead, an upper value to the integrated flux was determined within the 3σ confidence level. This was done by integrating the noise in the expected range of the signal −8 − 23 km/s. We find a value of 0.20 ± 0.07 K km/s, where the uncertainty is within 3σ, calculated for T_{mb}. We can compare this to the ratio of 6-5 and 3-2 lines in literature to determine the expected spread of change in flux, see Table **6.1**. First, we will have to convert the integrated intensities to integrated flux because of the different beam sizes for other telescopes and observing frequencies. We have used the conversion between integrated intensity (K km/s) and in-

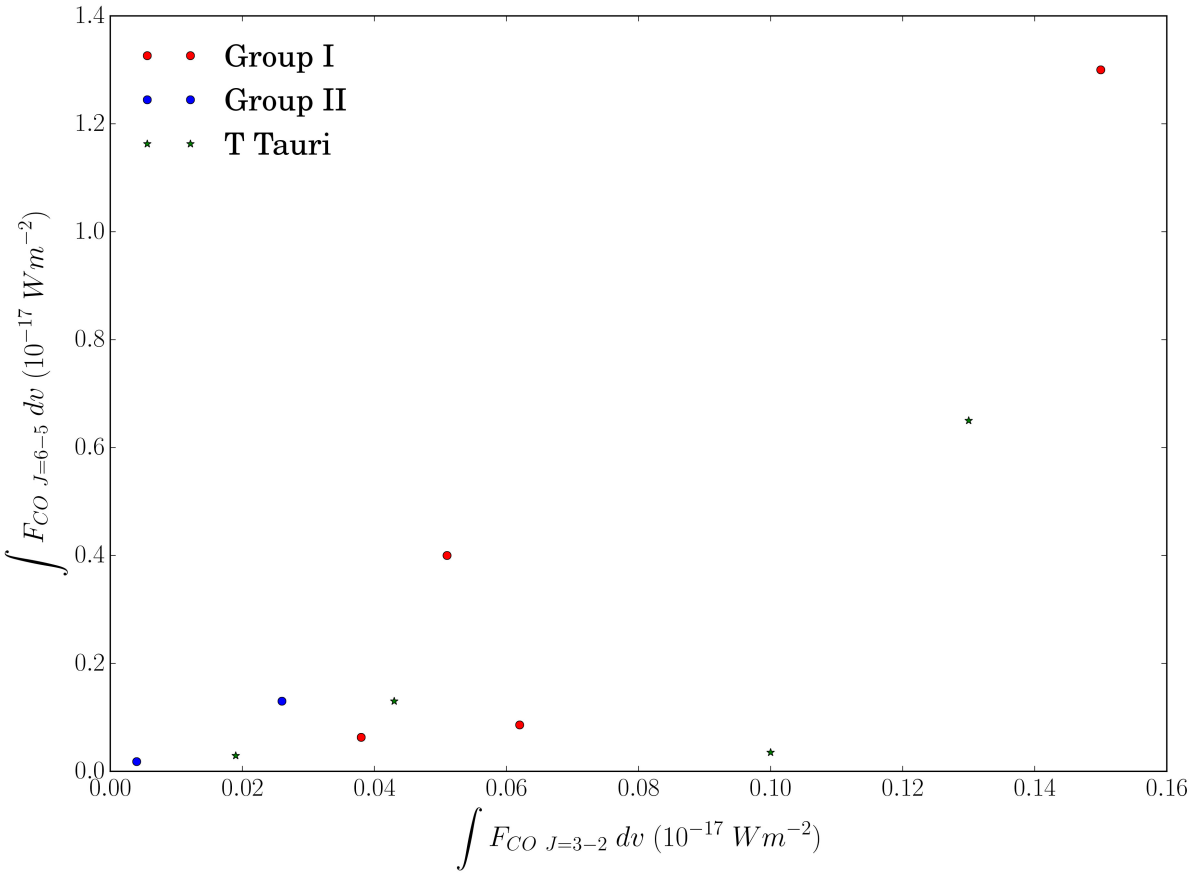

Figure 6.1: Flux ratios of disk stars with known values for the CO J=6-5 and CO J=3-2 line fluxes. An apparent dichotomy is seen, as Group I disks appear to have a substantial increase in CO J=6-5 flux as compared to Group II disks.

Table 6.1: Literature data on the CO rotational lines including the ratios, the integrated intensities have been converted to integrated fluxes.

Target	Type	$\int I_{COJ=3-2} dv$ (K km/s)	$\int I_{CO\ J=6-5} dv$ (K km/s)	$\frac{\int I_{CO\ J=6-5} dv}{\int I_{COJ=3-2} dv}$	$\int F_{COJ=3-2} dv$ ($10^{-17}\ Wm^{-2}$)	$\int F_{COJ=6-5} dv$ ($10^{-17}\ Wm^{-2}$)	$\frac{\int F_{CO\ J=6-5} dv}{\int F_{COJ=3-2} dv}$
DM Tau	T Tauri	5.43[a]	0.5[b]	0.09	0.019	0.029	1.5
HD100546	Herbig GI	4.0[h]	17.7[h]	4.0	0.15	1.3	8.7
HD104237	Herbig GII	0.11[c]	**0.25**[d]	2.5	0.0040	**0.018**	4.5
HD142527	Herbig GI	1.7[c]	1.5[b]	0.88	0.062	0.086	1.4
HD142666	Herbig GII	0.72[e]	-	-	0.016	-	-
HD144668	Herbig GII	7.2[c]	2.2[b]	0.31	0.026	0.13	5.0
HD169142	Herbig GI	1.7[e]	1.1[b]	0.65	0.038	0.063	1.7
HD97048	Herbig GI	1.4[c]	7.0[b]	5.0	0.051	0.40	7.8
IM Lup	T Tauri	4.7[f]	0.6[b]	0.13	0.10	0.035	0.35
TW Hya	T Tauri	0.86[g]	1.0[b]	1.2	0.043	0.13	3.0
V892 Tau	T Tauri	6.05[i]	4.6[b]	0.76	0.13	0.65	5.0

[a] **Öberg et al. 2011**, [b] **Kama et al. 2016**, [c] **Hales et al. 2014**, [d] **This work**, [e] **Dent et al. 2005**, [f] **van Kempen et al. 2007**, [g] **Fedele et al. 2016**, [h] **Fedele et al. 2013**, [i] **Panić and Hogerheijde 2009**

tegrated flux (Wm^{-2}) from **Fedele et al. (2016)**,

$$\int T_{mb} dv = 2k_B \frac{\nu^3}{c^3} \pi \left(\frac{HPBW}{2\sqrt{ln(2)}} \right)^2 \int T_{mb} dv \ \ [K\ km/s] \quad , \tag{6.1}$$

where k_B is the Boltzmann constant in Ws/K, ν the observing frequency in Hz, c the speed of light in m/s, and the HPBW the beam size in radians. These ratios are plotted in Fig. **6.1** to provide a better insight of the difference of group I, group II and T Tauri disks. T Tauri stars do not necessarily follow the same classification. It is still insightful to see how they compare. Though the sample size is too small to be decisive, an apparent dichotomy is seen.

Group II disks are self-shadowed and are thus colder than group I disks. The excitation temperature of CO J=6-5 is larger than for CO J=3-2. Hence, in the colder environments of the surface layers of group II disks, there is a smaller area where CO J=6-5 emission is probable in comparison to a group I disk. This dichotomy is thus expected, as from Fig. **6.1** group I disks appear to have a tendency to have a larger increase in CO J=6-5 flux with respect to the CO J=3-2 flux.

Since HD142666 is a group II disk, we will use the ratios of the available group II disks to find the expected integrated flux range. We find an expected range of (0.05-0.07)$\cdot 10^{-17}$ Wm^{-2}. From the integrated noise we can take the upper limit using the 3σ level to determine an upper value for the integrated flux of HD142666. The upper limit found is

$$\int F_{CO\ J=6-5} dv < 0.020 \cdot 10^{-17}\ Wm^{-2} \quad . \tag{6.2}$$

This value is not within the expected range. This is because our sample only contains 2 group II disks, which is not representative. Given the short integration time on this source, it is possible that the signal is buried in the noise. This is most likely the case as we do see a hint of a line, suggesting that the integrated flux cannot be unusually small.

7 Conclusions

For HD104237 we find from the 3σ line profiles a FWHM = 8.6 ± 1.4 km/s, $\int I_{CO\ J=6-5} dv$ = 0.25 ± 0.02 K km/s, Δv_{peak} = 4.39 ± 0.84, I_{peak} = 0.032 ± 0.005 K. The radial temperature distribution was determined for this disk, with T∼ 116 K at R = 85 ± 50 au and T∼ 33 K at R = 112 ± 51 au. This temperature distribution was compared to gas temperature radial profiles for several flaring angles from **Fedele et al. (2016)**. Large flaring angles (ψ = 0.15, 0.25) have a gas temperature that remains at ∼100 K for radii over 100 au, whereas with lower flaring angles (ψ = 0.05) the gas temperature drops to 40 K at a radius of 100 au. If we look at the minimum radius allowed by the uncertainty (35 au), we find from the radial profile that the gas temperature is ∼100 K which fits much better to our inferred temperature distribution. Furthermore, the brightness temperature of the source as calculated with the beam dilution factor is 3.4 K for a CO J=6-5 emitting region within a radius of 85 au. Taking again the minimum radius allowed (35 au), we find a brightness temperature of 27 K. This is still very small, and is likely due to the large uncertainties in our values for the radius, mass, distance and inclination. However, the fact that both the temperature profile as well as the brightness temperature give a more physical result when using a smaller outer radius, leads us to believe that we have underestimated the peak-separation in our analysis. A larger peak-separation would decrease the outer radius of emission leading to a higher brightness temperature and a better agreement with the radial profiles from **Fedele et al. (2016)**. It is possible that we have underestimated the peak-saparation in our analysis. The low resolutions that we had to bin to can diminish structure and the model fit is prone to error when applied to only a few data points.

For HD 142666 there was no 3σ detection. We did manage to determine an upper value of the integrated flux for this source, $\int F_{CO\ J=6-5} dv < 0.020 \cdot 10^{-17}$ Wm^{-2}. From the ratios of CO J=6-5 over CO J=3-2 for group II disks we expect the integrated flux to lie in the range (0.05-0.07)$\cdot 10^{-17}$ Wm^{-2}. The value of the integrated flux that we found does not lie in this range, which is due to the small sample size of group II disks. Because we do see a hint of a line, it is likely that the signal is hidden in the noise rather than being an unusually weak signal. The integration time on this source was 1.3 hours, with a $T_{rms} \approx 0.23$ K at a binsize of 1 km/s. If we want to obtain a reliable line profile with a signal-to-noise of 3 or higher for this binsize, we will need an integration time of 7-8 hours with APEX to reduce the T_{rms} to 0.01 K. At this binning the resulting line profile should give a result reliable enough to be used for comparison against numerical models.

8 | Acknowledgements

Special thanks to my supervisor I. Kamp for helping me throughout this project. Further gratitude goes out to M. Hogerheijde for explaining to me the basics of receivers and back-ends, and to Ü. Kavak for great help with the basics of GILDAS CLASS and my presentation slides.

Furthermore, I want to thank the organisers of the Summer School "Protoplanetary Disks: Theory and Modelling Meet Observations", for providing a wealth of knowledge on the subject of protoplanetary disks in just 15 very interesting papers, which I recommend to anyone with an interest in (and with a mathematical background of) astronomy and planet formation.

Based on observations collected at the European Organisation for Astronomical Research in the Southern Hemisphere under ESO programme 098.C-0562(A).

Bibliography

Baryshev, A. M., Hesper, R., Mena, F. P., et al. (2015). **The ALMA Band 9 receiver. Design, construction, characterization, and first light**. *A&A*, 577:A129.

Beckwith, S. and Sargent, A. (1987). **Interferometric images of ^{13}CO emission toward HL Tau.** In *Circumstellar Matter*, volume 122 of *IAU Symposium*, pages 81–83.

Beckwith, S., Sargent, A. I., Scoville, N. Z., Masson, C. R., Zuckerman, B., and Phillips, T. G. (1986). **Small-scale structure of the circumstellar gas of HL Tauri and R Monocerotis**. *ApJ*, 309:755–761.

Beckwith, S. V. W. and Sargent, A. I. (1993). **Molecular line emission from circumstellar disks**. *APJ*, 402:280–291.

Blondel, P. F. C. and Djie, H. R. E. T. A. (2006). **Modeling of PMS Ae/Fe stars using UV spectra**. *A&A*, 456:1045–1068.

Böhm, T., Catala, C., Balona, L., and Carter, B. (2004). **Spectroscopic monitoring of the Herbig Ae star HD 104237. I. Multiperiodic stellar oscillations**. *A&A*, 427:907–922.

Dent, W. R. F., Greaves, J. S., and Coulson, I. M. (2005). **CO emission from discs around isolated HAeBe and Vega-excess stars**. *MNRAS*, 359:663–676.

Dionatos, O. (2015). **Summer School on "Protoplanetary Disks: Theory and Modeling Meet Observations"**. *EPJ Web of Conferences*, 102.

Dominik, C. (2015). **Summer School on "Protoplanetary Disks: Theory and Modeling Meet Observations"**. *EPJ Web of Conferences*, 102.

Dominik, C., Dullemond, C. P., Waters, L. B. F. M., and Walch, S. (2003). **Understanding the spectra of isolated Herbig stars in the frame of a passive disk model**. *A&A*, 398:607–619.

Dullemond, C. P. and Dominik, C. (2004). **Flaring vs. self-shadowed disks: The SEDs of Herbig Ae/Be stars**. *A&A*, 417:159–168.

Dunhill, A. C., Cuadra, J., and Dougados, C. (2015). **Precession and accretion in circumbinary discs: the case of HD 104237**. *Monthly Notices of the Royal Astronomical Society*, 448:3545–3554.

Fang, M., van Boekel, R., Bouwman, J., Henning, T., Lawson, W. A., and Sicilia-Aguilar, A. (2013). **Young stars in ϵ Chamaleontis and their disks: disk evolution in sparse associations**. *A&A*, 549:A15.

Fedele, D., Bruderer, S., van Dishoeck, E. F., Hogerheijde, M. R., Panic, O., Brown, J. M., and Henning, T. (2013). **probing the radial temperature structure of protoplanetary disks with herschel/hifi**. *The Astrophysical Journal Letters*, 776(1):L3.

Fedele, D., van Dishoeck, E. F., Kama, M., Bruderer, S., and Hogerheijde, M. R. (2016). **Probing the 2D temperature structure of protoplanetary disks with Herschel observations of high-J CO lines**. *A&A*, 591:A95.

Garcia, P. J. V., Benisty, M., Dougados, C., Bacciotti, F., Clausse, J.-M., Massi, F., Mérand, A., Petrov, R., and Weigelt, G. (2013). **Pre-main-sequence binaries with tidally disrupted discs: the Brγ in HD 104237**. *Monthly Notices of the Royal Astronomical Society*, 430:1839–1853.

Garufi, A., Meeus, G., Benisty, M., Quanz, S. P., Banzatti, A., Kama, M., et al. (2017). **Evolution of protoplanetary disks from their taxonomy in scattered light: Group I vs. Group II**. *A&A*, 603:A21.

Grady, C. A., Woodgate, B., Torres, C. A. O., Henning, T., Apai, D., Rodmann, J., Wang, H., et al. (2004). **the environment of the optically brightest herbig ae star, hd 104237**. *The Astrophysical Journal*, 608(2):809.

Gundlach, B. and Blum, J. (2015). **the stickiness of micrometer-sized water-ice particles**. *The Astrophysical Journal*, 798(1):34.

Güsten, R., Nyman, L. Å., Schilke, P., Menten, K., Cesarsky, C., and Booth, R. (2006). **The Atacama Pathfinder EXperiment (APEX) - a new submillimeter facility for southern skies -**. *A&A*, 454:L13–L16.

Hales, A. S., De Gregorio-Monsalvo, I., Montesinos, B., Casassus, S., Dent, W. F. R., Dougados, C., et al. (2014). **A CO Survey in Planet-forming Disks: Characterizing the Gas Content in the Epoch of Planet Formation**. *AJ*, 148:47.

Herbig, G. H. (1960). **The Spectra of Be- and Ae-Type Stars Associated with Nebulosity**. *The Astrophysical Journal*, 4:337.

Hu, J. Y., Blondel, P. F. C., The, P. S., Tjin A Djie, H. R. E., de Winter, D., Catala, C., and Talavera, A. (1991). **IUE observations of the bright Herbig AE star HD 104237**. *A&A*, 248:150–154.

Hu, J. Y., The, P. S., and de Winter, D. (1989). **Photometric and spectroscopic study of three candidate Herbig Ae/Be stars - HD 37411, HD 100546, and HD 104237**. *A&A*, 208:213–218.

Kama, M., Bruderer, S., Carney, M., Hogerheijde, M., van Dishoeck, E. F., Fedele, D., et al. (2016). **Observations and modelling of CO and [C i] in protoplanetary disks. First detections of [C i] and constraints on the carbon abundance**. *A&A*, 588:A108.

Klein, B., Hochgürtel, S., Krämer, I., Bell, A., Meyer, K., and Güsten, R. (2012). **High-resolution wide-band fast Fourier transform spectrometers**. *A&A*, 542:L3.

Knude, J. and Hog, E. (1998). **Interstellar reddening from the HIPPARCOS and TYCHO catalogues. I. Distances to nearby molecular clouds and star forming regions**. *A&A*, 338:897–904.

Lee, C.-F., Li, Z.-Y., Ho, P. T. P., Hirano, N., Zhang, Q., and Shang, H. (2017). **Formation and Atmosphere of Complex Organic Molecules of the HH 212 Protostellar Disk**. *ArXiv e-prints*.

Meeus, G., Waelkens, C., and Malfait, K. (1998). **HD 139614, HD 142666 and HD 144432: evidence for circumstellar disks**. *A&A*, 329:131–136.

Meeus, G., Waters, L. B. F. M., Bouwman, J., van den Ancker, M. E., Waelkens, C., and Malfait, K. (2001). **ISO spectroscopy of circumstellar dust in 14 Herbig Ae/Be systems: Towards an understanding of dust processing**. *A&A*, 365:476–490.

Nomura, H., Tsukagoshi, T., Kawabe, R., Ishimoto, D., Okuzumi, S., Muto, T., et al. (2016). **ALMA Observations of a Gap and a Ring in the Protoplanetary Disk around TW Hya**. *Astrophysical Journal, Letters*, 819:L7.

Öberg, K. I., Qi, C., Wilner, D. J., and Andrews, S. M. (2011). **the ionization fraction in the dm tau protoplanetary disk**. *The Astrophysical Journal*, 743(2):152.

Panić, O. and Hogerheijde, M. R. (2009). **Characterising discs around Herbig Ae/Be stars through modelling of low-J ^{12}CO lines**. *A&A*, 508:707–716.

Pogodin, M. A., Cahuasqui, J. A., Drake, N. A., Hubrig, S., Schöller, M., Petr-Gotzens, M., et al. (2015). **Probing the Structure of the Accretion Region in a Sample of Magnetic Herbig Ae/Be Stars**. In Balega, Y. Y., Romanyuk, I. I., and Kudryavtsev, D. O., editors, *Physics and Evolution of Magnetic and Related Stars*, volume 494 of *Astronomical Society of the Pacific Conference Series*, page 175.

Polehampton, E. and Hafok, H. (2013). ***APEX Calibration and Data Reduction Manual***.

Testi, L., Birnstiel, T., Ricci, L., Andrews, S., Blum, J., Carpenter, J., Dominik, C., Isella, A., Natta, A., Williams, J. P., and Wilner, D. J. (2014). **Dust Evolution in Protoplanetary Disks**. *Protostars and Planets VI*, pages 339–361.

van Kempen, T. A., van Dishoeck, E. F., Brinch, C., and Hogerheijde, M. R. (2007). **Searching for gas-rich disks around T Tauri stars in Lupus**. *A&A*, 461:983–990.

Vieira, S. L. A., Corradi, W. J. B., Alencar, S. H. P., Mendes, L. T. S., Torres, C. A. O., Quast, G. R., Guimarães, M. M., and da Silva, L. (2003). **investigation of 131 herbig ae/be candidate stars**. *The Astronomical Journal*, 126(6):2971.

Vural, J., Kreplin, A., Kishimoto, M., Weigelt, G., Hofmann, K.-H., Kraus, S., Schertl, D., Dugué, M., Duvert, G., Lagarde, S., and Massi, F. (2014). **The inner circumstellar disk of the UX Orionis star V1026 Scorpii**. *A&A*, 564:A118.

Waters, L. B. F. M. (2015). **Summer School on "Protoplanetary Disks: Theory and Modeling Meet Observations"**. *EPJ Web of Conferences*, 102.

Woitke, P., Kamp, I., and Thi, W.-F. (2009). **Radiation thermochemical models of protoplanetary disks. I. Hydrostatic disk structure and inner rim**. *A&A*, 501:383–406.

Appendices

A | Appendix A: Figures

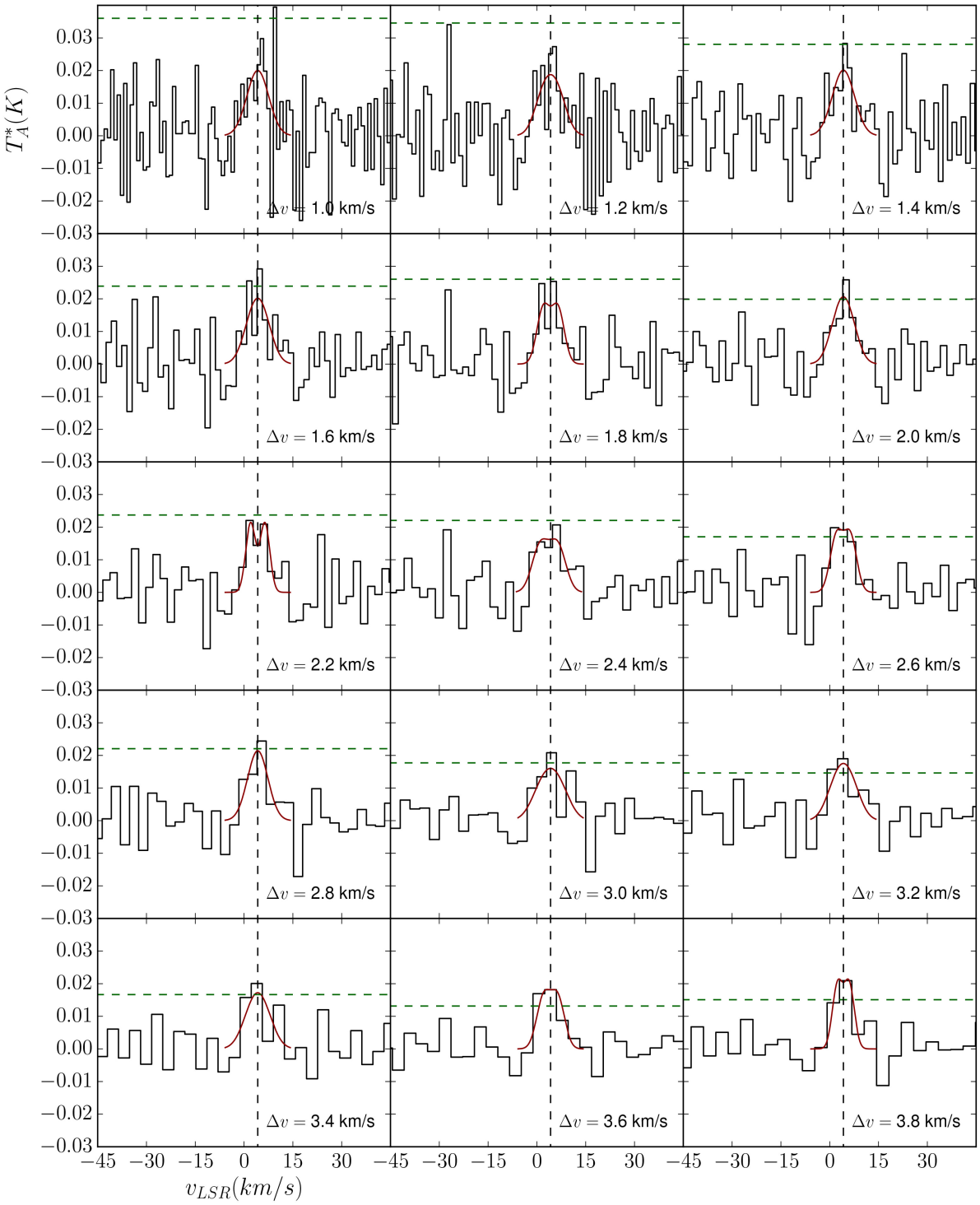

Figure A.1: Analysis of various bin sizes for HD104237. The green dotted line is the three sigma level, blue is the one sigma level. The signal is in good agreement with the literature value of the velocity with respect to the local standard of rest of the system (black dotted line).

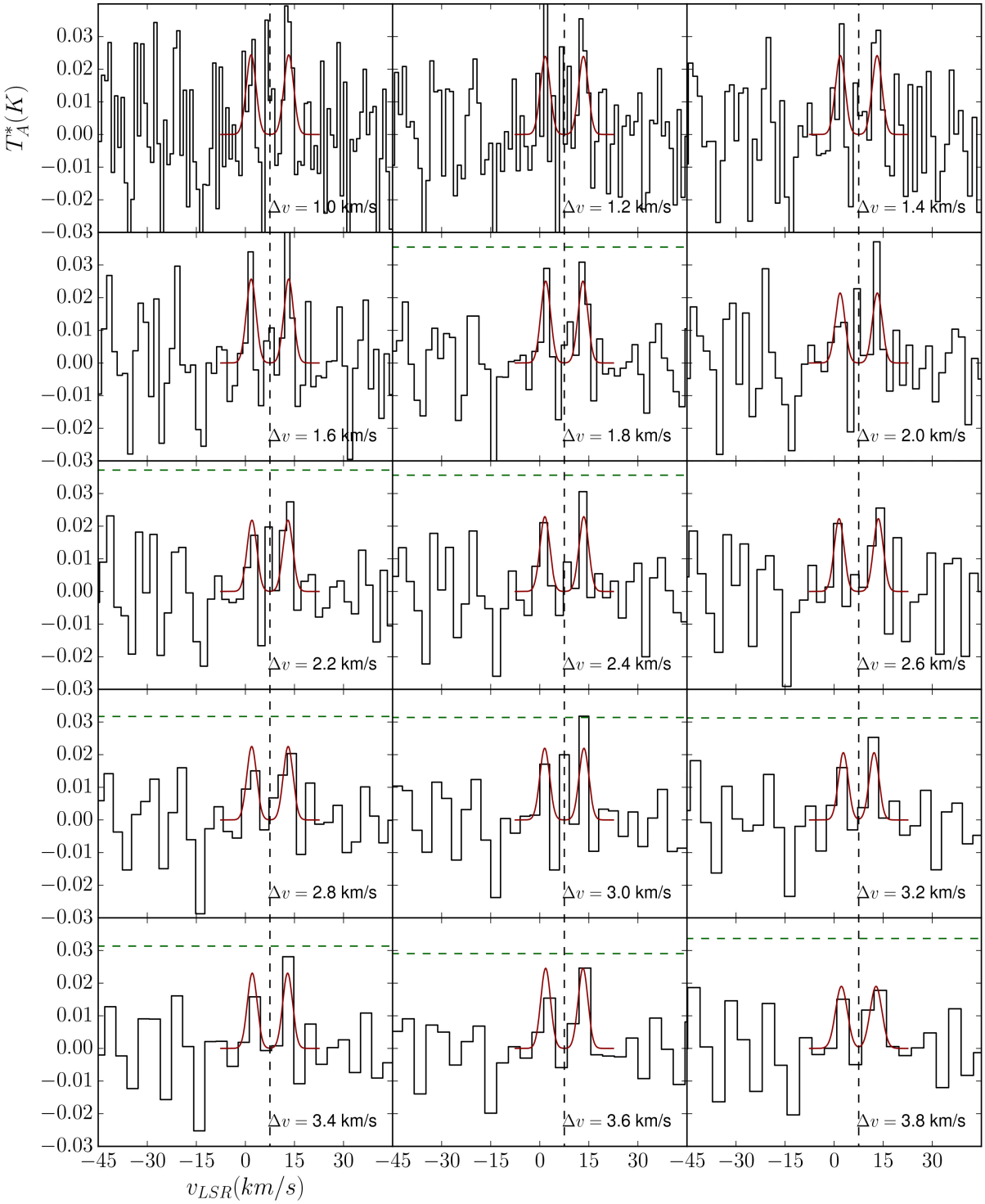

Figure A.2: Analysis of various bin sizes for HD142666. The green dotted line is the three sigma level. The black dotted line represents the expected location of the signal given the v_{LSR} range in **Panić and Hogerheijde 2009**. No 3σ detection is seen.